

CHAPTER 5. DEMONSTRATION OF IMAGE-PROCESSING TECHNIQUES

In the previous chapter, we developed image-processing tools that will allow us to analyze each mode of a radiating structure independently. Ultimately, we would like to use these tools to understand new antennas whose radiating mechanisms are not yet explained. However, we first need to demonstrate that the tools provide accurate results. By investigating a canonical problem, we can compare it to the established theory and obtain an overall verification of the image-processing tools. Through the analysis of a known structure, we also might be able to develop guidelines as to where the tools are applicable and understand their limitations.

Our selection of a canonical case is governed by two main constraints. First, the time and spectral behavior of the benchmark structure needs to be well described by theory. Additionally, the canonical case needs to be capable of supporting two or more modes. One electromagnetic structure that meets both of the above constraints is a rectangular waveguide. Used as the first type of guiding structure for transporting microwave energy, the operation of a waveguide can be found in most electromagnetic textbooks. We can obtain multi-mode behavior in a waveguide by choosing an appropriate operating frequency. In addition, the geometry of a rectangular waveguide lends itself well to computational modeling and simulation.

This chapter provides an illustrative example of the image-processing tools that we developed in Chapter 4. Using FDTD simulation results for an open-ended rectangular waveguide, we can demonstrate the mode-discrimination characteristics of

the image-processing tools. A quick review of waveguide theory is provided in Section 5.1 and the geometry of the FDTD computational model is presented in Section 5.2. Finally, the data is visualized in Section 5.3 and compared to rectangular waveguide theory.

5.1 Waveguide Theory

The geometry of a rectangular waveguide is shown in Figure 5-1. The walls are comprised of perfect electric conductor and the inside of the guide is filled with air. For analytical purposes, the guide is assumed to be infinite in length. Due to the boundary conditions on the waveguide walls, transverse electromagnetic (TEM) field configurations are not supported. However, the structure does support transverse electric (TE) and transverse magnetic (TM) modes. In this chapter, we will only provide solutions for TE modes since they are excited at much lower operating frequencies than TM modes.

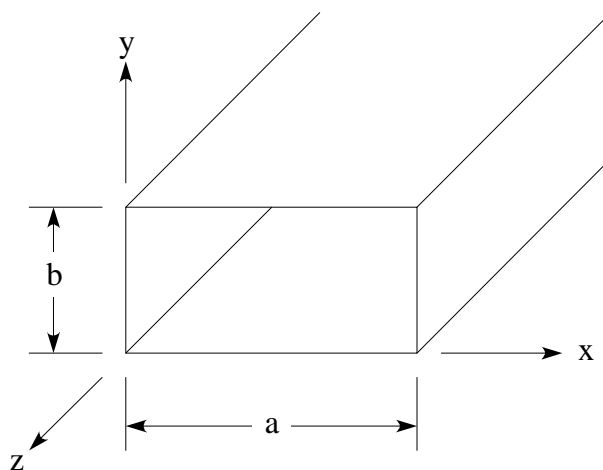


Figure 5-1. Geometry of rectangular waveguide.

Balanis uses the vector potential approach to find the following solution for the \vec{E} - and \vec{H} -field distributions of the TE_z modes [8]:

$$\begin{aligned} E_x &= A_{mn} \frac{k_y}{e} \cos(k_x x) \sin(k_y y) e^{-jk_z z} \\ E_y &= -A_{mn} \frac{k_x}{e} \sin(k_x x) \cos(k_y y) e^{-jk_z z} \\ E_z &= 0 \end{aligned} \quad (5-1)$$

$$\begin{aligned} H_x &= A_{mn} \frac{k_x k_z}{\omega \mu e} \sin(k_x x) \cos(k_y y) e^{-jk_z z} \\ H_y &= A_{mn} \frac{k_y k_z}{\omega \mu e} \cos(k_x x) \sin(k_y y) e^{-jk_z z} , \\ H_z &= -jA_{mn} \frac{k_c^2}{\omega \mu e} \cos(k_x x) \cos(k_y y) e^{-jk_z z} \end{aligned} \quad (5-2)$$

where k_x , k_y , and k_z are wavenumbers given by

$$\left. \begin{aligned} k_x &= \frac{mp}{a} = \frac{2p}{l_x} & m = 0, 1, 2, \dots \\ k_y &= \frac{np}{b} = \frac{2p}{l_y} & n = 0, 1, 2, \dots \end{aligned} \right\} m = n \neq 0 \quad (5-3)$$

$$k_z = b \sqrt{1 - \left(\frac{l}{l_c}\right)^2} = b \sqrt{1 - \left(\frac{f_c}{f}\right)^2}$$

In the above equations, f and f_c represent the operating frequency and cutoff frequency, respectively. Inspecting the equation for k_z , we see that it takes on real values when $f \geq f_c$ and imaginary values when $f < f_c$. Substituting this result into equations (5-1) and (5-2), it becomes evident that the modes whose cutoff frequencies are below the operating frequency will propagate in the z -direction. Additionally, modes where the cutoff

frequency is greater than the operating frequency will decay exponentially with distance. These modes are commonly referred to as evanescent modes. Typically, one is only interested in the propagating modes since the evanescent modes are only present in the regions around the electromagnetic source. Balanis provides the following formulas for the cutoff frequencies and their corresponding cutoff wavenumbers [8]:

$$(f_c)_{mn} = \frac{1}{2p \sqrt{\mu\epsilon}} \sqrt{\left(\frac{mp}{a}\right)^2 + \left(\frac{np}{b}\right)^2} \quad \left. \begin{array}{l} m = 0, 1, 2, \dots \\ n = 0, 1, 2, \dots \end{array} \right\} m = n \neq 0 \quad (5-4)$$

$$(k_c)_{mn} = \sqrt{k_x^2 + k_y^2} = \frac{2p}{l_c}. \quad (5-5)$$

Equations (5-1) and (5-2) give the field distributions of the propagating modes. Since we will be visualizing these distributions, it would be helpful to know what they look like. Figure 5-2 illustrates the spatial-domain field patterns for the first 18 TE_z and TM_z modes in a rectangular waveguide. The k-space diagram shown in Figure 5-3 shows the distribution of spectral energy for the first few modes. Spectral energy exists only at discrete points in k-space and is represented with dots; the other areas are very small in magnitude (theoretically zero).

This concludes our brief review of waveguide theory. At this point, we should have a clear understanding of the field distributions in both the spatial-domain and in k-space. In the next section we will discuss the FDTD model that generates the data. Then in Section 5.3 we will analyze the data and compare the results with the ideas presented here.

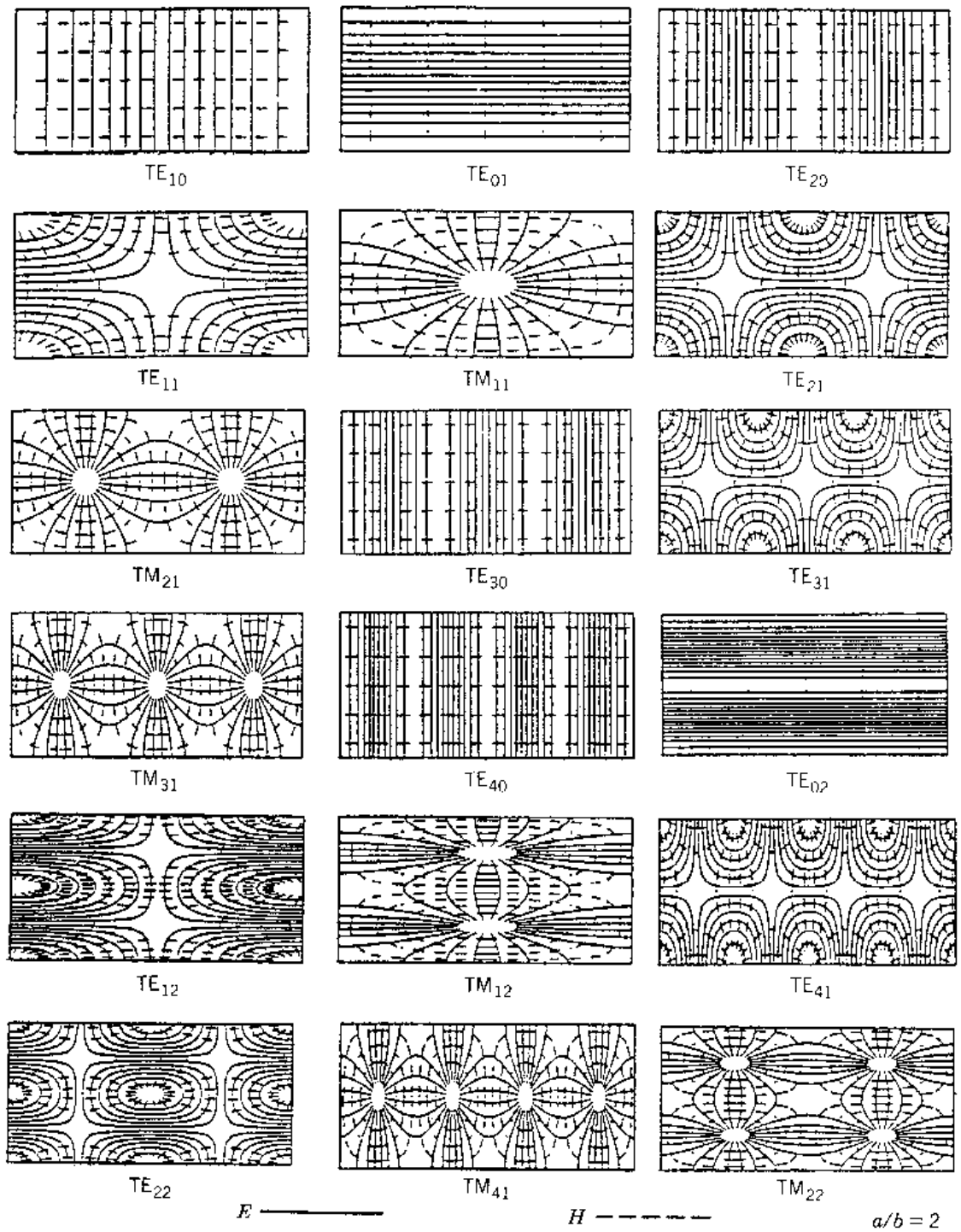


Figure 5-2. Field patterns for the first 18 modes in a rectangular waveguide [24].

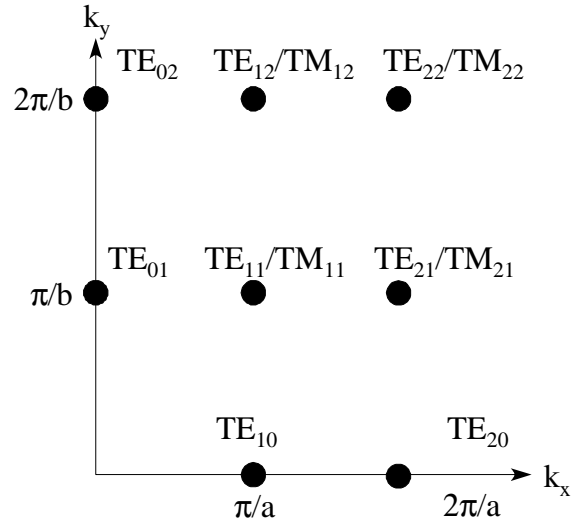


Figure 5-3. Spectral domain distribution of various propagating modes.

5.2 Description of Computational Model

In this section, we provide the details of the FDTD model used to generate the data in our example. The x-y and y-z plane views of the computational model are shown in Figures 5-4 and 5-5, respectively. The guide parameters and cell dimensions are as follows:

$$\begin{aligned}
 & \left. \begin{aligned} a &= 7.214 \text{ cm} \\ b &= 3.404 \text{ cm} \end{aligned} \right\} \text{WR284 waveguide} \\
 & \Delta x = 0.3136522 \text{ cm} \\
 & \Delta y = 0.3094546 \text{ cm} \\
 & \Delta z = 0.3 \text{ cm}
 \end{aligned} \quad . \quad (5-6)$$

The open-ended waveguide radiates into a computational space that is terminated with an absorbing boundary condition. Since the radiated energy does not reflect back towards the structure, this arrangement accurately simulates free-space operation.

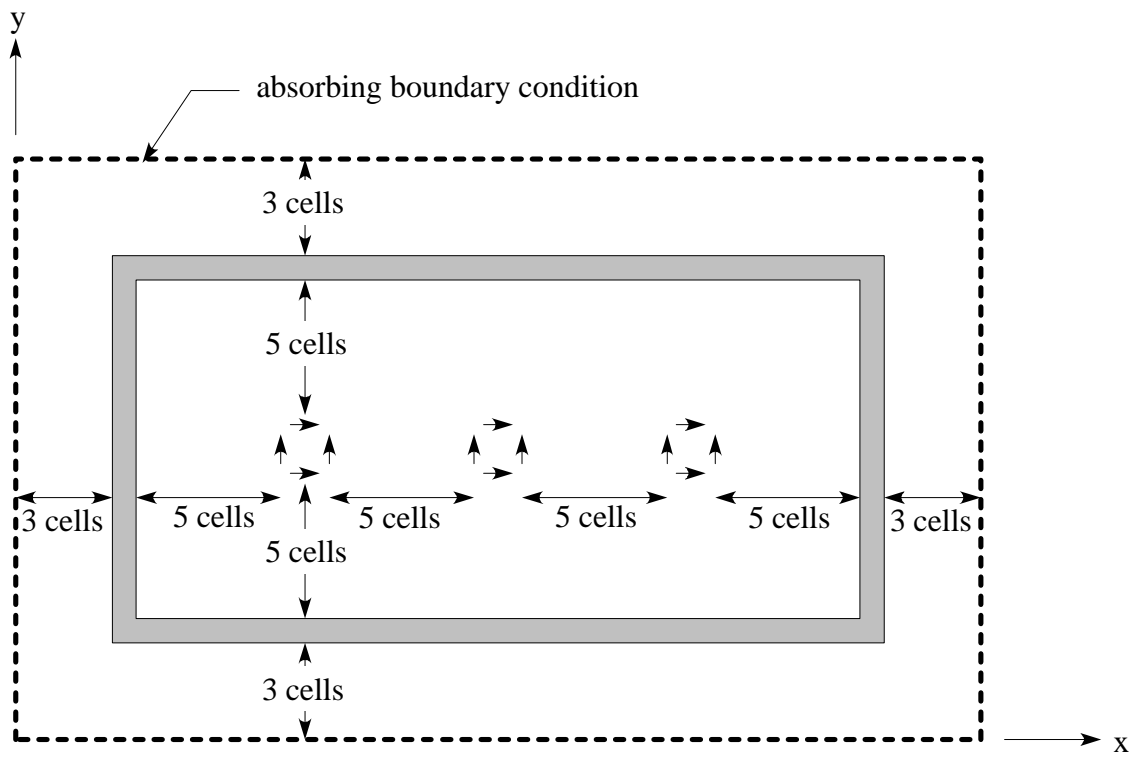


Figure 5-4. X-Y plane of FDTD computational space.

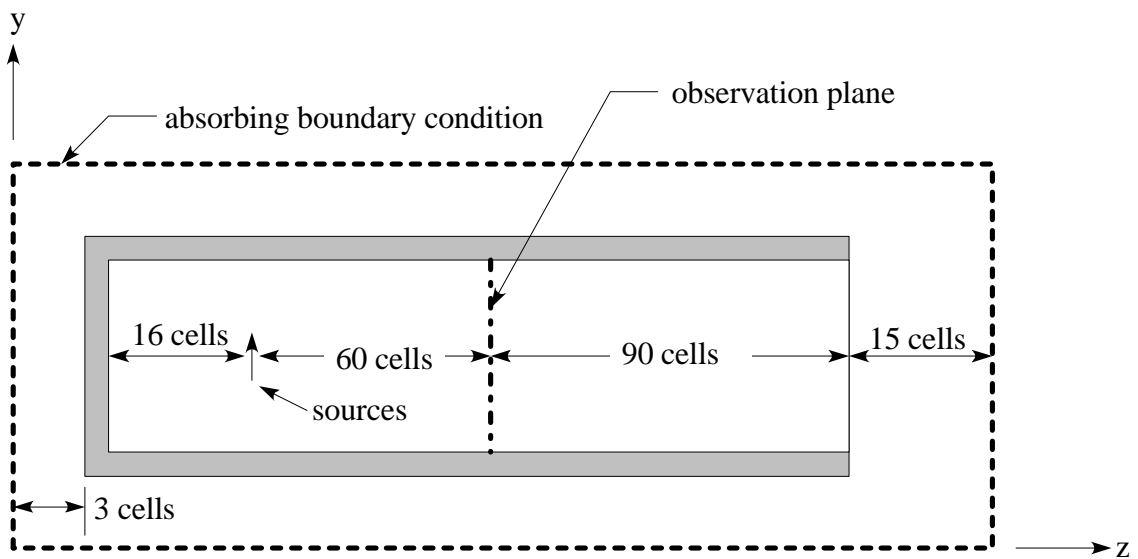


Figure 5-5. Y-Z plane of FDTD computational space.

The above figures also show the placement of the feed sources in the computational space. A number of infinitesimal dipoles, which represent coaxial probe feeds, are arranged so that they couple energy to the first three modes (TE_{10} , TE_{20} , and TE_{01}). This is accomplished by orienting each of the linear probes so that its length is parallel to the electric field lines of the various modes [8]. Thus, the horizontal probes will excite the TE_{01} mode, while the vertical probes couple energy to the TE_{10} and TE_{20} modes. We elected to excite the waveguide for both dominant and mixed-mode operation ($f=3$ GHz and 4.7 GHz). Using equations (5-3) and (5-4), we can calculate the wavenumbers for the propagating modes in the guide. The results are given below

3.0 GHz Operation

$$\begin{aligned} TE_{10} \text{ Mode: } & k_x = 43.55 \text{ rad/m} \\ & k_y = 0 \text{ rad/m} \\ & k_z = 45.35 \text{ rad/m} \end{aligned}$$

4.7 GHz Operation

$$\begin{aligned} TE_{10} \text{ Mode: } & k_x = 43.55 \text{ rad/m} \\ & k_y = 0 \text{ rad/m} \\ & k_z = 88.35 \text{ rad/m} \\ TE_{20} \text{ Mode: } & k_x = 87.10 \text{ rad/m} \\ & k_y = 0 \text{ rad/m} \\ & k_z = 46.01 \text{ rad/m} \\ TE_{01} \text{ Mode: } & k_x = 0 \text{ rad/m} \\ & k_y = 92.29 \text{ rad/m} \\ & k_z = 34.43 \text{ rad/m} \end{aligned}$$

The FDTD computational engine was run on a Pentium 133 personal computer with 64 Megabytes of memory. The total execution time was approximately 12 hours. In the next section we will present animations of the electric field distributions for the waveguide. In addition, the image-processing techniques developed in Chapter 4 will be applied to provide a mode-discrimination. These results will also be presented in the form of animations.

5.3 Discrimination of Modes

In this section, we will analyze the results from the above FDTD model of an open-ended rectangular waveguide. To begin with we will show the results using only the visualization methods that were developed in Chapter 2. Then we will apply the mode-discrimination tools of Chapter 4 and visualize the result so that we can demonstrate the effectiveness of the image-processing techniques. In both cases, the visualization network is analogous to that given in the example of Chapter 3 (see Figure 3-8).

In the previous section we simulated the waveguide for both dominant and mixed-mode excitations. The dominant mode results are shown in Figures 5-6 and 5-7. In the x-y plane the data shows a cosine distribution in the x-direction and a uniform distribution along the y-axis. This result matches exactly with the theoretical field distributions given in Section 5.1. In the y-z plane, we see that a standing wave pattern is set up along the length of the waveguide. This result is expected since the guide is terminated with an open-circuit. If we watch closely, there is a small traveling wave component that is evident. This is due to the fact that the waveguide is radiating. Some energy is lost due to radiation so the return wave is smaller in amplitude than the incident wave. In these animations we can clearly observe the field distributions of the dominant mode. Visualizing the data for the mixed-mode excitation in Figure 5-8, we can see that there are two modes present. Although it is quite difficult to use the mind's eye to separate the effect of each mode. This type of analysis requires the mode-discrimination tools that we developed in Chapter 4.

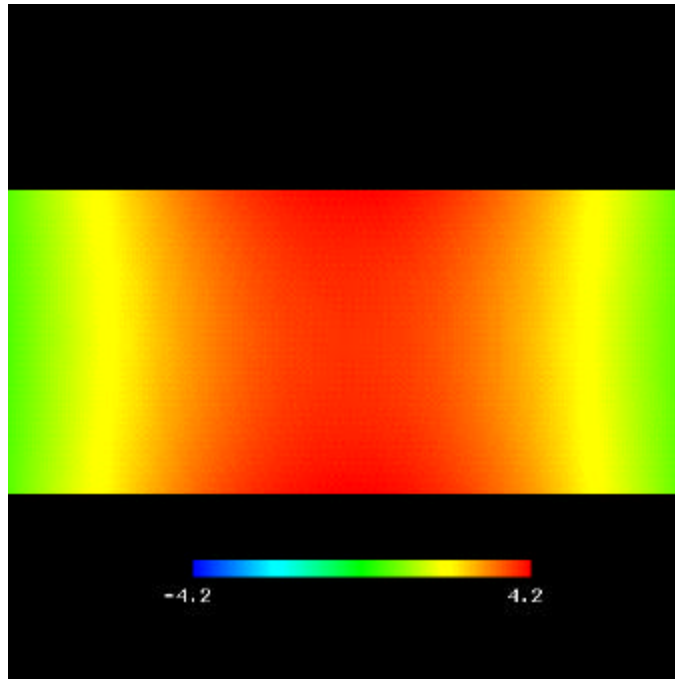


Figure 5-6. X-Y plane, dominant mode ($f=3.0$ GHz) electric field distribution.

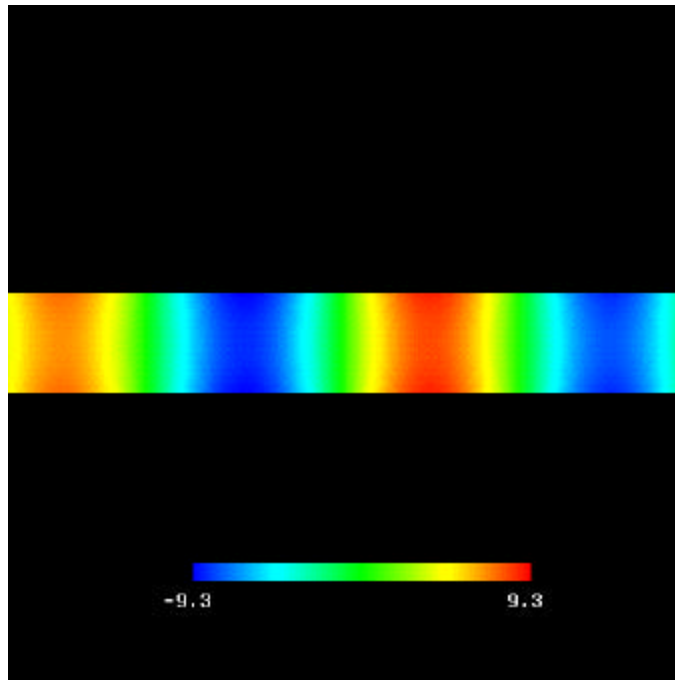


Figure 5-7. Y-Z plane, dominant mode ($f=3.0$ GHz) electric field distribution.

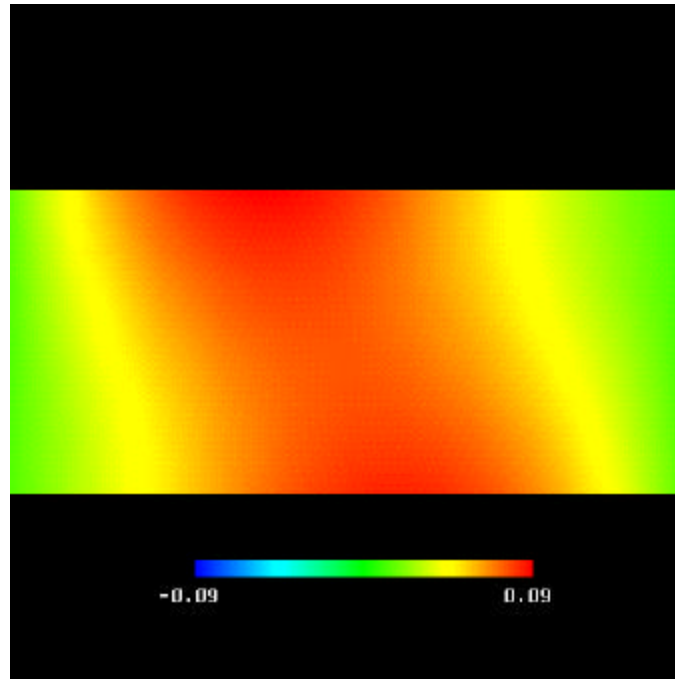


Figure 5-8. X-Y plane, mixed-mode ($f=4.7$ GHz) electric field distribution.

Before we can apply the mode-discrimination tools we need to address two important issues. First, it is necessary to ensure that the data is sampled finely enough to satisfy the Nyquist rate. This is fairly easy to show using the low-pass characteristic of the waveguide (propagating modes exist only for $(f_c)_{mn} \leq f$). Using equation (5-3), we can determine the maximal value of each propagating wavenumber (k_x, k_y, k_z). Plugging these values into equation (4-3) provides an upper bound for the sampling interval in each dimension. The results below show that the data is adequately sampled in all three spatial dimensions.

$$\begin{aligned}
 \Delta x &= 0.314 \text{ cm} \leq 3.6 \text{ cm} \\
 \Delta y &= 0.309 \text{ cm} \leq 3.4 \text{ cm} \\
 \Delta z &= 0.3 \text{ cm} \leq 3.5 \text{ cm}
 \end{aligned}
 \tag{5-7}$$

The second issue we need to consider is the size of the data window. For the dominant mode fields, the data window is only a half-wavelength wide. If we extend the data using the assumed periodicity of the FFT, we obtain a rectified sine wave. Thus the sampled data will be incorrect every other half-cycle. Fortunately, in this case we can artificially extend the data set using properties of the waveguide structure. Since the walls of the waveguide are comprised of perfect electric conductor, the fields inside see an environment that repeats periodically. This property is used in the field of antenna measurements to simulate infinite arrays [25]. Essentially, we can image the data window about each of the conducting walls as illustrated in Figure 5-9. Now if the data set is extended using the assumed periodicity of the FFT, we see that the sampled data is correct everywhere in the spatial-domain. From this discussion we can see that one of the limitations of the image-processing techniques is that they require a data window that is at least a wavelength in width. We are able to circumvent the problem in this case using intimate knowledge of the structure being analyzed. However, this may not be the case for a generalized structure.

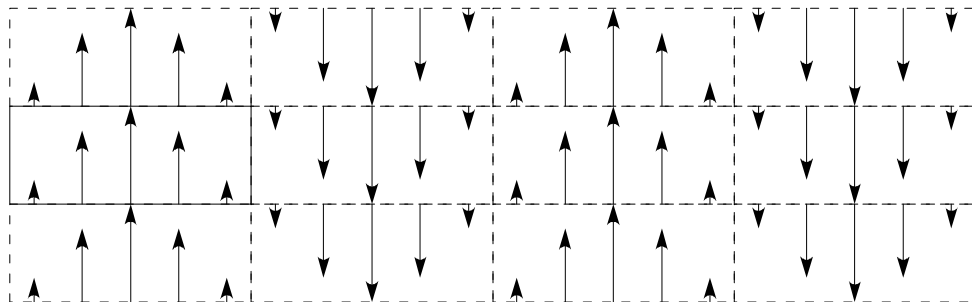


Figure 5-9. Example of imaging method used in waveguide problem.

Now, if we use the FFT to convert the y-component data to the spectral domain, we see that the result matches the theory quite well (see Figure 5-10). Here we should note that the TE_{01} mode does not show up since it is purely polarized in the x-direction. Using the Gabor window that was defined in Chapter 4, we can filter each of the modes and convert them back to the spatial-domain. These results are shown in Figures 5-11 and 5-12.

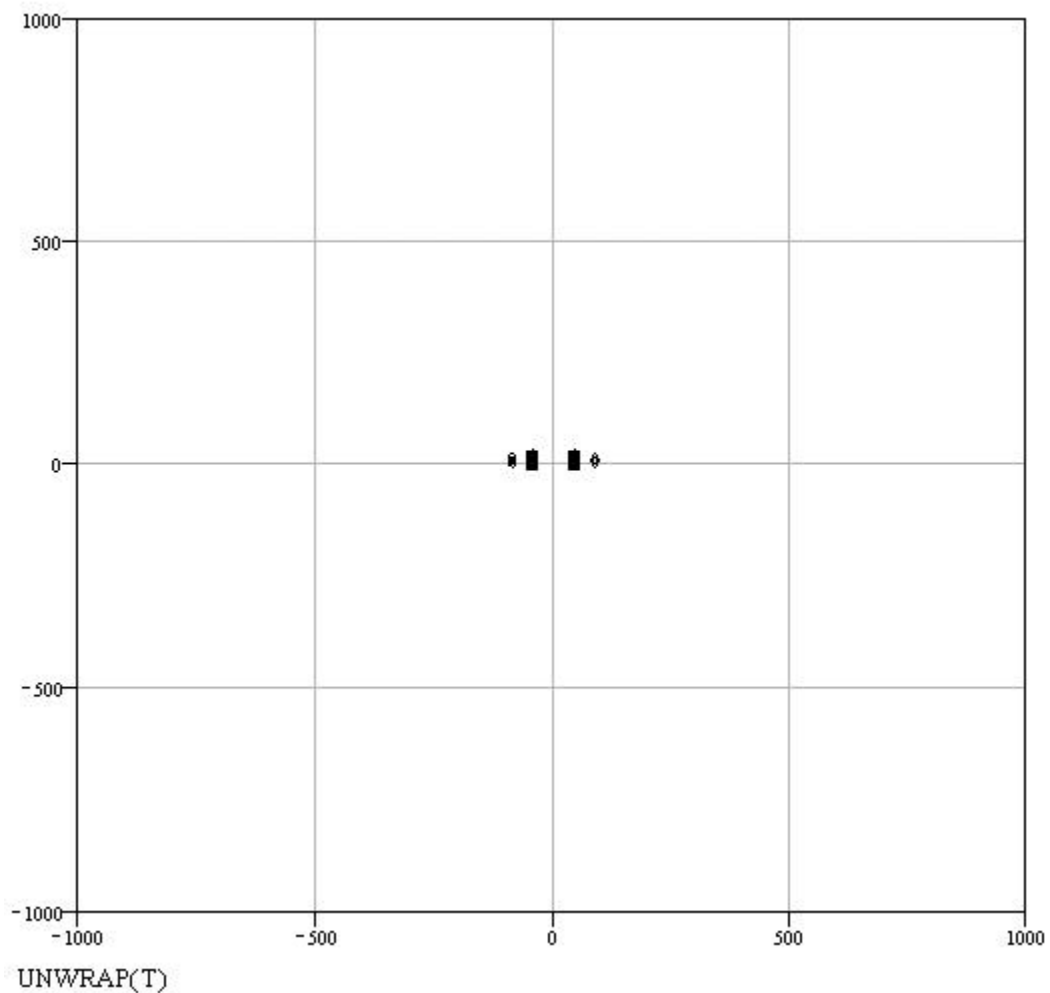


Figure 5-10. Spectral domain content of mixed-mode data.

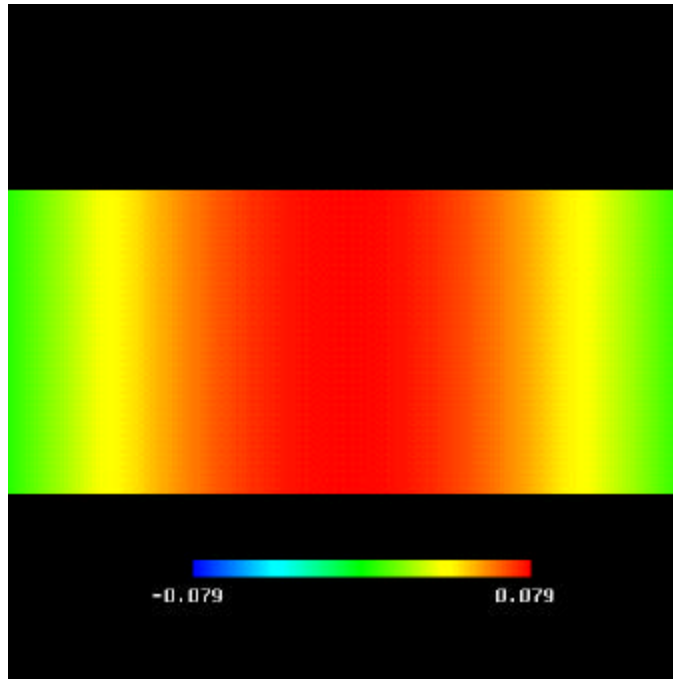


Figure 5-11. X-Y plane, TE₁₀ filter applied to mixed-mode data.

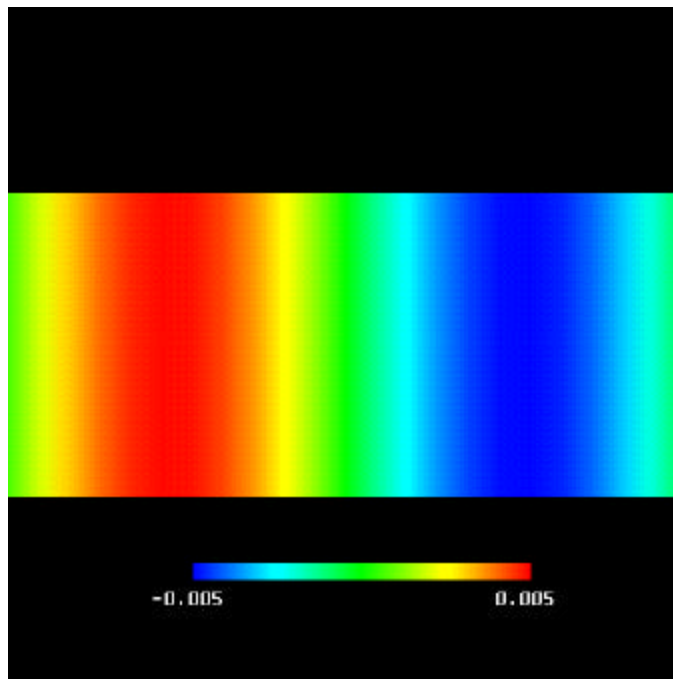


Figure 5-12. X-Y plane, TE₂₀ filter applied to mixed-mode data.

By viewing the modes independently, we can clearly identify the modal field distributions, which match the theoretical formulations exactly. From the color scale, we can see that the amplitude of the TE_{20} mode is much smaller than the TE_{10} mode. This result proves that the Gabor filter can accurately discriminate between modes with different propagation constants, even when the amplitude of one mode is much smaller than the other. In addition, by applying the mode-discrimination techniques to the above canonical case, we are able to identify a limitation of the method. The data window needs to be at least a wavelength in extent. This is a very important piece of information that might have gone unnoticed if we did not know the distribution of the expected outputs. Now that we have a better understanding of the visualization and image-processing tools, we are ready to apply them to an unknown radiating structure. This is beyond the scope of this thesis, although some guidelines and suggestions will be given in the next chapter.